J. Fluid Mech. (1997), *vol.* 335, *pp.* 213–232

Finite-wavelength instability in a horizontal liquid layer on an oscillating plane

By A. C. OR

Department of Mechanical and Aerospace Engineering, University of California, Los Angeles, CA 90095-1597, USA

(Received 5 February 1996 and in revised form 3 October 1996)

The linear stability of a thin liquid layer bounded from above by a free surface and from below by an oscillating plate is investigated for disturbances of arbitrary wavenumbers, a range of imposed frequencies and selective physical parameters. The imposed motion of the lower wall occurs in its own plane and is unidirectional and time-periodic. Long-wave instabilities occur only over certain bandwidths of the imposed frequency, as determined by a long-wavelength expansion. A fully numerical method based on Floquet theory is used to investigate solutions with arbitrary wavenumbers, and a new free-surface instability is found that has a finite preferred wavelength. This instability occurs continuously once the imposed frequency exceeds a certain threshold. The neutral curves of this new finite-wavelength instability appear significantly more complex than those for long waves. In a certain parameter regime, folds occur in the finite-wavelength stability limit, giving rise to isolated unstable regions. Only synchronous solutions are found, i.e. subharmonic solutions have not been detected. In Appendix A, we provide an argument for the non-existence of subharmonic solutions.

1. Introduction

Yih (1968) studied the hydrodynamic stability of a thin liquid layer bounded from below by a flat horizontal wall that performs unidirectional oscillations in its own plane. The upper surface of the layer is a deformable free surface. Based on a long-wave expansion, Yih found that long waves can become unstable for sufficiently large-amplitude oscillations within regions corresponding to separated bandwidths of the imposed frequency. As the frequency increases, an increasingly large amplitude for the oscillatory motion is required to excite the instability.

Yih's instability for this unsteady flow appears to be related to the long-wavelength instability occurring for the steady flow of a liquid on an inclined plane (see e.g. Yih 1963) because both involve the effect of shear on a deflection of a surface along which the shear stress is prescribed (see Kelly *et al*. 1989 and Smith 1990 for detailed discussions of the instability mechanism for the falling film problem). For Yih's oscillating plane problem, no analysis has been reported so far for arbitrary wavenumbers. The main aim of the present paper is to fill this gap in our knowledge. As reported first by Or & Kelly (1995*a*), finite-wavenumber instabilities can not only occur but can be more unstable than the long-wavenumber instabilities.

Several recent studies can be viewed as being related to Yih's problem. Woods & Lin (1995) have extended the problem of a liquid layer flowing down an incline so

as to allow the lower wall of the layer to perform oscillatory motions in a direction perpendicular to its own plane. In this case, Faraday waves are excited due to the effective modulation of gravity along with the usual long-wavelength surface waves (Yih 1963) modulated by the oscillation. In more recent work (Lin, Chen & Woods 1996), the effects of tangential oscillations have been investigated but results are given only for the case of nearly vertical walls. Coward & Renardy (1995) have reported some results for the two-layer horizontal problem with a mean flow, but only for the case of small-amplitude oscillations. From a different viewpoint, considerable effort in understanding thermocapillary instabilities of the Marangoni–Bénard type has been made recently in association with NASA's experimental efforts in the area of microgravity fluid physics. For that problem, a heated layer of liquid with a free surface is examined. This paper is a by-product of an ongoing effort by the author and Professor R.E. Kelly to understand the control of thermocapillary instabilities by means of an imposed oscillatory shear; see, e.g. Or & Kelly (1995*b*). The present results, however, are relevant to a much larger class of problems involving liquid films and may be related to wave-induced instability of an interface.

The long-wave expansion is reviewed first to present the critical Reynolds number for long waves as obtained by Yih (1968) and then extended to obtain the next order correction in the expansion

$$Re = Re_0 + Re_2 k^2 + \dots . \tag{1.1}$$

Besides giving information about the curvature of the neutral stability boundaries, the value of Re_2 is used later to locate points where finite-wavelength neutral curves branch off the long-wavelength neutral curves.

During the course of several other related studies involving the stability of unsteady shear flows (Kelly & Hu 1994; Schulze & Davis 1995; Or & Kelly 1995*b*), the authors have noted their unsuccessful attempts to find subharmonic solutions. Yih's (1968) long waves are of the synchronous type as well. One might argue that the analysts simply have not located the right regions in parameter space for the occurrence of subharmonic solutions. However, in Appendix A to this paper, it is argued that subharmonic solutions simply do not exist for a class of equations that includes the present ones.

2. Mathematical formulation

The configuration for the problem (see figure 1) consists of a horizontal liquid layer of thickness h. The liquid is viscous, incompressible, and isothermal. The horizontal extent of the liquid is assumed infinite. The upper boundary is a deformable free surface; the bottom is a rigid wall, which performs a unidirectional oscillation in its plane. The momentum equation and the continuity equation describing the system are

$$\partial_t \boldsymbol{v} + \boldsymbol{v} \cdot \nabla \boldsymbol{v} = -\frac{1}{\rho_0} \nabla p + \nu \nabla^2 \boldsymbol{v}, \tag{2.1a}$$

$$\nabla \cdot \boldsymbol{v} = 0, \tag{2.1b}$$

where $\boldsymbol{v}$ is the liquid's velocity and p is its pressure. The rigid wall condition is given by

$$\boldsymbol{v} = \boldsymbol{i} U_0 \cos \omega t \quad \text{at } z = h, \tag{2.2a}$$

where $\boldsymbol{i}$ is a unit vector in the x-direction, ω is the frequency and U_0 is the modulation amplitude of velocity. The primitive form of the free surface normal stress, tangential

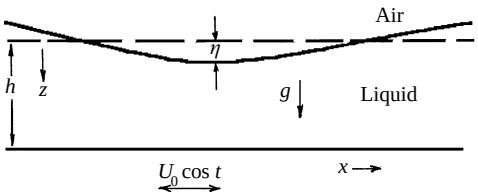

FIGURE 1. The geometric configuration.

stress and kinematic conditions, respectively, at $z = \eta(x, y, t)$ where η measures the surface deformation, are

$$\boldsymbol{n} \cdot \boldsymbol{T} \cdot \boldsymbol{n} = p_0 - \sigma \left(\frac{1}{R_1} + \frac{1}{R_2} \right), \tag{2.2b}$$

$$\boldsymbol{t}_i \cdot \boldsymbol{T} \cdot \boldsymbol{n} = 0, \tag{2.2c}$$

where $i = 1, 2$ and

$$\partial_t \eta + \boldsymbol{v} \cdot \nabla \eta = \boldsymbol{v} \cdot \boldsymbol{n}. \tag{2.2d}$$

In the above, $\boldsymbol{T}$ is the stress tensor of the three-dimensional space and, approximately, $\boldsymbol{n} = (-\eta_x, -\eta_y, 1)$ (inward to fluid), $\boldsymbol{t}_1 = (1, 0, \eta_x)$, and $\boldsymbol{t}_2 = (0, 1, \eta_y)$. These are vectors normal and parallel to the interface. On the right-hand side of the normal stress equation, p_0 is the air pressure, σ is the surface tension, and R_1 and R_2 are known as the principal radii of curvature. Derivations of surface boundary conditions based on the above primitive form of equations can be found in Joseph & Renardy (1993, § III-2).

The basic state is a periodic flow parallel to the wall. By introducing U_0 as a characteristic velocity, the equilibrium layer thickness h as the length scale and ω^{-1} as the time scale, we obtain the governing equations as follows. For this case the surface is non-deformed, and the exact flow solution is given by

$$\boldsymbol{v}_s(z, t) = \boldsymbol{i} U_0 \{ \phi_c(z) \cos t + \phi_s(z) \sin t \}, \tag{2.3}$$

where the two expressions for the coefficients ϕ_c and ϕ_s are

$$\phi_c(z) = \frac{1}{2} \left\{ \frac{\cosh(1 + \mathrm{i})\beta z}{\cosh(1 + \mathrm{i})\beta} + \frac{\cosh(1 - \mathrm{i})\beta z}{\cosh(1 - \mathrm{i})\beta} \right\}, \tag{2.4a}$$

$$\phi_s(z) = \mathrm{i} \frac{1}{2} \left\{ \frac{\cosh(1 + \mathrm{i})\beta z}{\cosh(1 + \mathrm{i})\beta} - \frac{\cosh(1 - \mathrm{i})\beta z}{\cosh(1 - \mathrm{i})\beta} \right\}, \tag{2.4b}$$

where β will be defined shortly. The stability equations are derived from the momentum and continuity equations by perturbing the basic state, dropping all nonlinear disturbance terms and eliminating the disturbance pressure. Both horizontal velocity components, u and v, are then eliminated in favour of the vertical velocity component, w, through the use of the continuity equation. The resulting system is scalar and has only w and η as dependent variables. Since there are no lateral boundaries, a functional dependence of $\mathrm{e}^{\mathrm{i}kx}$ is assumed for all dependent variables, where k is the

wavenumber for the assumed two-dimensional disturbances. After some manipulation we obtain

$$(2\beta^2\partial_t - (\partial_{zz} - k^2))(\partial_{zz} - k^2)w = -\mathrm{i}kRe(\phi_c \cos t + \phi_s \sin t)(\partial_{zz} - k^2)w + \mathrm{i}kRe(\phi_c'' \cos t + \phi_s'' \sin t)w. \tag{2.5}$$

The wall boundary conditions are now

$$w = \partial_z w = 0 \text{ at } z = 1. \tag{2.6a}$$

The free-surface conditions are linearized with respect to the equilibrium level. The conditions for the normal and tangential stresses, as well as the kinematic condition, are, respectively,

$$(2\beta^2\partial_{zt} - \partial_{zzz} + 3k^2\partial_z)w - 2k^2\left(\chi + \frac{k^2}{2\psi}\right)\eta = -\mathrm{i}kRe(\phi_c \cos t + \phi_s \sin t)\partial_z w, \tag{2.6b}$$

$$\partial_{zz} w + k^2 w = \mathrm{i}kRe(\phi_c'' \cos t + \phi_s'' \sin t)\eta, \tag{2.6c}$$

$$2\beta^2\partial_t \eta - w = -\mathrm{i}kRe(\phi_c \cos t + \phi_s \sin t)\eta, \tag{2.6d}$$

at $z = 0$. The expressions for the non-dimensional parameters appearing in (2.5, 2.6*a–d*) are

$$2\beta^2 = \frac{\omega h^2}{\nu},\ Re = \frac{U_0 h}{\nu},\ \chi = \frac{gh^3}{2\nu^2},\ \psi = \left(\frac{\rho\nu^2}{\sigma h}\right). \tag{2.7}$$

The physical quantities appearing above but not yet defined are: acceleration due to gravity g; density of liquid ρ; surface tension σ and kinematic viscosity ν. The term $2\beta^2$ represents the dimensionless imposed frequency, and β is the ratio of the layer depth to a Stokes layer thickness. The Reynolds number Re is a measure of the modulation amplitude, and the parameter χ is a non-dimensional measure of gravity, sometimes referred to as the Galileo number. It corresponds to the Reynolds number for a liquid film flowing due to gravity. The parameter ψ involves the surface tension and is related to the crispation number by the Prandtl number; it is used because there are no thermal effects. Also, ψ and χ are used instead of the conventional Bond number and, say, χ or ψ, in order to have two parameters, one of which solely contains g while the other solely contains σ. These parameters are convenient for microgravity research. On the other hand, the Weber number and Froude number are not used here because we want Re to be the only parameter containing the modulation amplitude, U_0, and to define the other parameters so as to be appropriate for the unmodulated case.

3. The long-wavelength expansion

The long-wavelength expansion is reviewed briefly in order to present Yih's (1968) result for the value of Re_0 corresponding to neutrally stable long-wavelength disturbances and also because Yih's results have been extended to higher order. For sufficiently small k, w, η and Re can be expanded as

$$w(z,t) = k(w_0 + kw_1 + k^2 w_2 + k^3 w_3 + k^4 w_4 + \ldots), \tag{3.1a}$$

$$\eta(z,t) = \eta_0 + k\eta_1 + k^2\eta_2 + k^3\eta_3 + k^4\eta_4 + \ldots, \tag{3.1b}$$

$$Re = Re_0 + k^2 Re_2 + \ldots, \tag{3.1c}$$

where Re is understood to be the Reynolds number for neutrally stable disturbances. At each order of k, the dependent variables can be separated into temporally sinusoidal functions multiplied by functions of z. The following form of representation is appropriate for the first few terms:

$$w_0 = \mathrm{i}Re_0(\hat{w}_0 \cos t + \check{w}_0 \sin t),\ \eta_1 = \mathrm{i}Re_0(\hat{\eta}_1 \cos t + \check{\eta}_1 \sin t), \tag{3.2a}$$

$$w_1 = Re_0^2(\overline{w}_1 + \hat{w}_1 \cos 2t + \check{w}_1 \sin 2t),\ \eta_2 = Re_0^2(\overline{\eta}_2 + \hat{\eta}_2 \cos 2t + \check{\eta}_2 \sin 2t). \tag{3.2b}$$

This form represents a synchronous response and is dictated by the forcing at the wall. In the complex form above, it should be noted that switching from the real to the imaginary parts introduces nothing new except for a shift in t. Factors associated with Re_0 appear at each order of expansion of the dependent variables because k not only enters the equations by itself but also in combination with Re in the modulation terms. Two solvability conditions arise via the mean terms generated at orders k^2 and k^4, which determine values of Re_0 and Re_2, respectively. The following complex notations are introduced for further simplifications:

$$\Phi = \phi_c + \mathrm{i}\phi_s,\ W_k = \hat{w}_k + \mathrm{i}\check{w}_k,\ N_{k+1} = \hat{\eta}_{k+1} + \mathrm{i}\check{\eta}_{k+1},\ k = 0, 1, 2.$$

The balances at each order of k are now described.

(i) *Zeroth-order*. After inspecting the governing equation and boundary conditions, we conclude that at $O(k^0)$ the velocity is zero and η_0 is constant, corresponding to a static spatially periodic deflection of the free surface. As a normalization condition, we impose $\eta_0 = 1$ in the subsequent results.

(ii) *First-order*. From here on, the balance at each order poses a fourth-order boundary-value problem. At $O(k^1)$, the governing equation is

$$\mathrm{i}2\beta^2 \mathrm{D}^2 W_0 + \mathrm{D}^4 W_0 = 0, \tag{3.3a}$$

where D denotes an ordinary derivative with respect to z, subject to boundary conditions

$$W_0 = \mathrm{D}W_0 = 0 \tag{3.3b}$$

at $z = 1$ and

$$\mathrm{D}^3 W_0 + \mathrm{i}2\beta^2 \mathrm{D}W_0 = 0,\ \mathrm{D}^2 W_0 - \Phi''(0) = 0 \tag{3.3c}$$

at $z = 0$. This flow is clearly generated via the shear-stress boundary condition for the lowest-order disturbed free surface, as seen by (3.3*d*). Although this boundary-value problem can be solved analytically in a reasonably straightforward manner, the algebra becomes tedious for the higher-order boundary-value problems and so a numerical approach is then used. For consistency, the above problem is also solved numerically by a tau method, using Chebyshev polynomials in the z-direction (see § III(c) of Joseph & Renardy 1993 for details concerning this method). The numerical discretization yields the following matrix equation,

$$\boldsymbol{A}\boldsymbol{w}_0 = \boldsymbol{q}.$$

where the vector $\boldsymbol{w}_0$ represents the Chebyshev coefficients. The matrix equation can be inverted to give $\boldsymbol{w}_0$. Having evaluated W_0, N_1 is then given by

$$N_1 = \frac{\mathrm{i}}{2\beta^2}(W_0 - \Phi(0)). \tag{3.3d}$$

At this order, Re remains undetermined. The driving term $\Phi''(0)$ arising at this order from the deflection of the shear-free surface is small at both low and high values of β^2.

(iii) *Second-order mean field.* Mean terms arise at $O(k^2)$ due to the in-phase interactions of the basic flow and disturbance terms, as well as to the horizontal hydrostatic pressure associated with the lowest-order surface deflection. The first solvability condition is determined from the mean equation at this order, which is associated with the following boundary-value problem:

$$\mathrm{D}^4\overline{w}_1 = -\tfrac{1}{2}(\phi_c \mathrm{D}^2\hat{w}_0 + \phi_s \mathrm{D}^2\check{w}_0) + \tfrac{1}{2}(\phi_c''\hat{w}_0 + \phi_s''\check{w}_0), \tag{3.4a}$$

with boundary conditions at $z = 1$

$$\overline{w}_1 = \mathrm{D}\overline{w}_1 = 0 \tag{3.4b}$$

and at $z = 0$

$$\mathrm{D}^3\overline{w}_1 = -\frac{2\chi}{Re_0^2} - \tfrac{1}{2}(\phi_c \mathrm{D}\hat{w}_0 + \phi_s \mathrm{D}\check{w}_0), \tag{3.4c}$$

$$\mathrm{D}^2\overline{w}_1 = -\tfrac{1}{2}(\phi_c''\hat{\eta}_1 + \phi_s''\check{\eta}_1), \tag{3.4d}$$

and

$$\overline{w}_1 = -\tfrac{1}{2}(\phi_c\hat{\eta}_1 + \phi_s\check{\eta}_1). \tag{3.4e}$$

Equation (3.4*c*) is the only equation which contains Re_0; it can be used to evaluate Re_0 because the remaining equations form a non-singular inhomogeneous matrix equation for $\overline{w_1}$, which can be readily inverted. We remark that the solvability condition in (3.4*a–e*) is obtained from the redundancy of the inhomogeneous boundary-value problem considered here, rather than from Fredholm's alternative. To compare with Yih's stability criterion, we define the quantity $L(\beta)$ as

$$L(\beta) = -(\mathrm{D}^3\overline{w}_1 + \tfrac{1}{2}(\phi_c \mathrm{D}\hat{w}_0 + \phi_s \mathrm{D}\check{w}_0))_{z=0}, \tag{3.5}$$

where $L(\beta)$ is tabulated and plotted in Yih's table 1 and figure 2. Equation (3.4*c*) can then be expressed as

$$\frac{2\chi}{Re_0^2} - L(\beta) = 0, \tag{3.6}$$

which can be rewritten as

$$L(\beta) = Fr^{-2},$$

where Fr denotes the Froude number. There is obviously no solution for $L < 0$. For $L > 0$, we have

$$Re_0 = \left(\frac{2\chi}{L(\beta)}\right)^{1/2} \tag{3.7}$$

for a neutrally stable solution. The criterion for instability

$$Re_0 > \left(\frac{2\chi}{L(\beta)}\right)^{1/2}$$

originally appeared in Yih's analysis as the expression $L(\beta) > Fr^{-2}$. Re_0 increases as χ increases because gravity then exerts an increasingly strong effect upon the deflection of the free surface, which is required for the instability. From Yih (1968, figure 2), $L(\beta)$ has a maximum near $\beta = 1$, and so the minimum value of Re_0 for a given value of χ occurs when the Stokes flow thickness is approximately equal to the depth of the layer. If we had used a similar long-wavelength analysis for $Re = 0$ in order to find the decay rate using a diffusive time scale, we would have found a decay rate proportional to $k^2\chi$, corresponding to a monotonic decay of the lowest-order

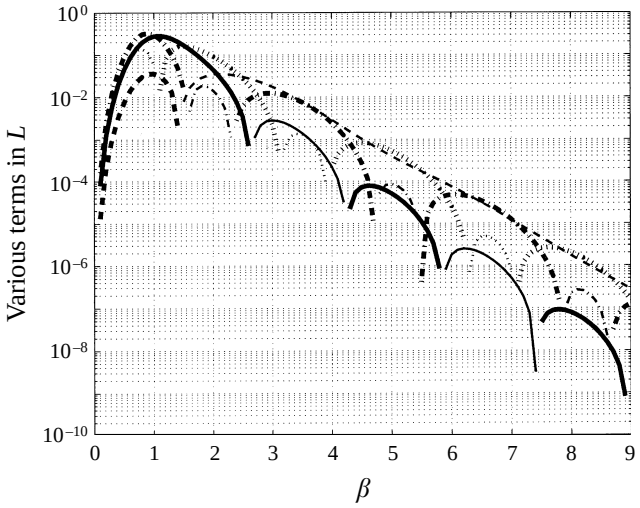

FIGURE 2. A plot showing $L(\beta)$ and the relative contributions of the individual terms in $L(\beta)$ as functions of β. For description of curves see text.

free-surface deflection via diffusion. Here the advective terms appearing on the right of (2.6*b*) act to counteract the effects of diffusion, presumably in a manner akin to that discussed by Smith (1990) for the falling film problem.

The expansion was carried to $O(k^4)$ in (3.1*a*) and $O(k^3)$ in (3.1*b*). As a result, Re_2 was determined during the solution for $\overline{w}_3(z)$, again by means of a solvability condition. However, the situation is more complicated at this order because Re_2 is contained in the governing equation and all the boundary conditions, unlike the problem involving Re_0. Nonetheless, the value of Re_2 is again obtained by solving the inhomogeneous matrix equation arising from use of the Chebyshev tau method when a redundant boundary condition occurs.

The oscillatory Stokes flow in a liquid layer becomes unstable to both long-wave and finite-wavenumber disturbances in the presence of free-surface deformation. The value of Re_2 controls both the curvature of the neutral curves and, as we shall see, is used to locate the point at which the finite-wavenumber neutral curves bifurcate from the long-wavelength neutral curves. In this way, the long-wavelength analysis serves as a valuable complement to the fully numerical approach. The basic flow and the disturbance field interact and generate a mean field, through which the energy of the basic flow amplifies the disturbance field. The mechanism for the instabilities can be understood better by examining the two solvability conditions in the long-wave expansion. The long-wave instability is relatively simple to understand in terms of the normal-stress condition at $z = 0$, by studying the relative importance of terms in $L(\beta)$ in (3.5). For a neutrally stable solution to be possible only over a finite β interval, L has to change sign. There are three terms in L: $-\mathrm{D}^3\overline{w}_1$, $-\frac{1}{2}\phi_c\mathrm{D}\hat{w}_0$ and $-\frac{1}{2}\phi_s\mathrm{D}\check{w}_0$. All three terms arise from p in the normal-stress expression, after p is eliminated by substituting from the two horizontal momentum equations. The first is a diffusive term; the second and third are Reynolds stress type terms. These three terms are shown, respectively, in the dashed, dashed-dotted and dotted curves in figure 2, in which a logarithmic scale is used for the ordinate. The heavy curves show the positive segments of the curves, whereas the thinner curves show the absolute values of the portions of curves where the values are negative. The solid curves

represent the sum of these three terms. The heavy solid curve represents a positive L for which a neutral solution is possible. The thin solid curve represents a negative L and therefore no neutral solution is possible. The actual curves are continuous but exhibit rapid changes in the regions where sign changes occur. Since the curves are generated at a β increment of 0.1, such rapid variations are not captured in figure 2. The results, though, show that the diffusive term $-\mathrm{D}^3\overline{w}_1$ is positive at about $\beta \leqslant 1.4$ and becomes negative afterward. It therefore promotes a neutral solution only at low β. The second term $-\frac{1}{2}\phi_c \mathrm{D}\hat{w}_0$ is positive over wider ranges of β than where it is negative. However, for $\beta > 1.4$, the slightly larger negative contribution of $-\mathrm{D}^3\overline{w}_1$ over the positive contribution of $-\frac{1}{2}\phi_c \mathrm{D}\hat{w}_0$ renders this latter term too weak by itself to generate the instability at the values of Re_0 determined (see § 5). For $\beta > 1.4$, the main contribution to the heavy solid curve comes from the term $-\frac{1}{2}\phi_s \mathrm{D}\check{w}_0$ which slightly overbalances the diffusive term. A similar evaluation of the non-homogeneous terms arising in the equation for $\overline{w}_3$ was made but will not be reported here for brevity. The results can be obtained from the author.

As pointed out by an anomymous reviewer of this paper, synchronicity is a necessary condition for the long-wavelength expansion. At $O(k)$, the right-hand side of boundary condition (2.6*c*) necessarily requires $\sigma_i = 0$. The condition is preserved as one carries on to the higher order. For arbitrary wavelength, synchronicity for a certain matrix time-dependent ordinary differential equation is demonstrated in Appendix A.

4. The fully numerical method

In the fully numerical method, (2.5) is solved directly subject to (2.6*a–d*). The z-dependence is again expanded in terms of Chebyshev polynomials. The difference now is that time-dependent amplitudes are involved and must be determined. The asymmetric boundary conditions are treated by Lanczos' tau method (Gottlieb & Orszag 1981, p. 11). Since the Chebyshev polynomials (modes) in general do not satisfy the boundary conditions, in the tau method the dependent variable is represented by $N_t + k$ Chebyshev functions, where the governing partial differential equation provides N_t ordinary differential equations with time-dependent coefficients, upon expansion and averaging with each Chebyshev function. The boundary conditions on both sides of the layer provide the rest of the k ordinary differential equations to close the system.

The numerical procedure yields an infinite sequence of difference matrix equations with time as the independent variable, shown symbolically as (A1) in Appendix A. Instead of solving a truncated augmented system, we solve the sequence of equations by a successive elimination method which is described in Appendix B. The method is based on an iterative approach using the Newton–Raphson method.

Most of the solutions computed here use 28 Fourier modes and 14 Chebyshev modes. The convergence test used is that, by increasing each of the Fourier and Chebyshev modes by 2, the converged iterate changes by less than 2%. All our computations are done in MATLAB.

5. Results

In this section we present both results of the long-wave expansion and of the fully numerical method. The long-wave results are obtained by extending Yih's findings to the $O(k^2)$ term in (3.1*c*). While these results can also be computed by the fully

numerical method, parameter sweeps can be done with the long-wave results in a significantly faster fashion than with only the fully numerical method, in which the wavenumber is an internal parameter to be searched for over a large band of values in order to locate the minima of *Re*. Owing to the large number of solutions required to construct a neutral curve, we only report two representative cases here with parameters selected on the basis of findings from the long-wave results: (i) $\psi = 0.05$ and $\chi = 1.0$ and (ii) $\psi = 0.5$ and $\chi = 0.3$. A wide variety of liquids, ranging from water to silicon oil, have ρ on the order of 1 g cm^{-3} and σ on the order of 10–10^2 dyne cm^{-1}. Here we let $\rho = 1.0$, $\sigma = 30$. The earth-bound gravity is 981 cm s^{-1}. Based on the definitions of χ and ψ in (2.7), for case (i) we obtain $h = 5.5 \times 10^{-2}$ cm and $v = 0.29$ cm^2 s^{-1}; and for case (ii) we have $h = 0.1$ cm and $v = 1.2$ cm^2 s^{-1}. A way to find an experimental liquid in this viscosity range is by mixing more viscous with less viscous miscible liquids. The other way is by heating a thicker oil since v decreases with temperature.

For case (i) we first present the combined long-wavelength and finite-wavelength results. We then locate the set of branch points at which the finite-wavenumber neutral curves appear by varying both ψ and χ in the long-wavelength analysis. Case (ii) is done more selectively; we focus mainly on certain interesting features. After studying the neutral curves and stability boundaries, we then turn to some analysis of the unstable disturbances' mode shapes for both cases, focusing primarily on the steady components of the disturbances.

In figure 3(*a*), we show three U-shaped neutral curves, which represent the stability boundaries for Yih's long-wave solution. These curves are obtained from the first solvability condition. Note that the ordinate has a logarithmic scale. As demonstrated by Yih (1968), the long-wavelength instability is controlled by the Froude number and β. Thus, from (3.7), we conclude that the family of U-shaped neutral curves is unchanged with respect to χ if $Re/\chi^{1/2}$ is used as the ordinate.

On the family of U-curves, the solid portions of the curves represent stability boundaries of the most dangerous long-wavelength unstable modes. They are therefore the physically preferred ones, corresponding to the lowest critical *Re*. The dashed portions of the U-curves are not associated with criticality due to competition from the new finite-k instability, whose neutral boundaries are shown by oblique lines emerging from the U-curves at branch points. In figure 3(*a*), which corresponds to case (i), each branch point is shown as a solid circle on each U-curve. The set of monotonic neutral curves associated with the finite-k instability have critical wavenumbers that vary with the imposed frequency. Figure 3(b) shows the variation with β of the critical wavenumber, k_c, along each monotonic neutral curve. As β decreases from above, $k_c \to 0$ at the branch points. As β becomes larger, the k_c of the higher branches become smaller and smaller. They seem to tend to zero asymptotically. On the third branch shown, $k_c \approx 0.03$ at $\beta = 10$. The vertical shape of this finite-k neutral mode closely resembles that of the long-wave solution (see figure 8).

We make a comparison between the approximate long-wave and the fully numerical results in figure 4, and it is clear that very substantial error can occur by use of the long-wave expansion results for cases for which a finite-wavelength instability can be critical. The region studied is near the first branch point at $\beta = 2.563$, and we use the same figure to discuss what happens in the vicinity of this branch point. The lower solid neutral curve corresponds to $\beta = 2.5625$. In this case, we clearly see that *Re* increases monotonically with k. The upper solid curve for $\beta = 2.5640$, however, has a minimum at $k = 0.24$. The curve connecting all the minima for various β in this range near 2.563 produces the dashed-dotted curve, which is the stability limit, or

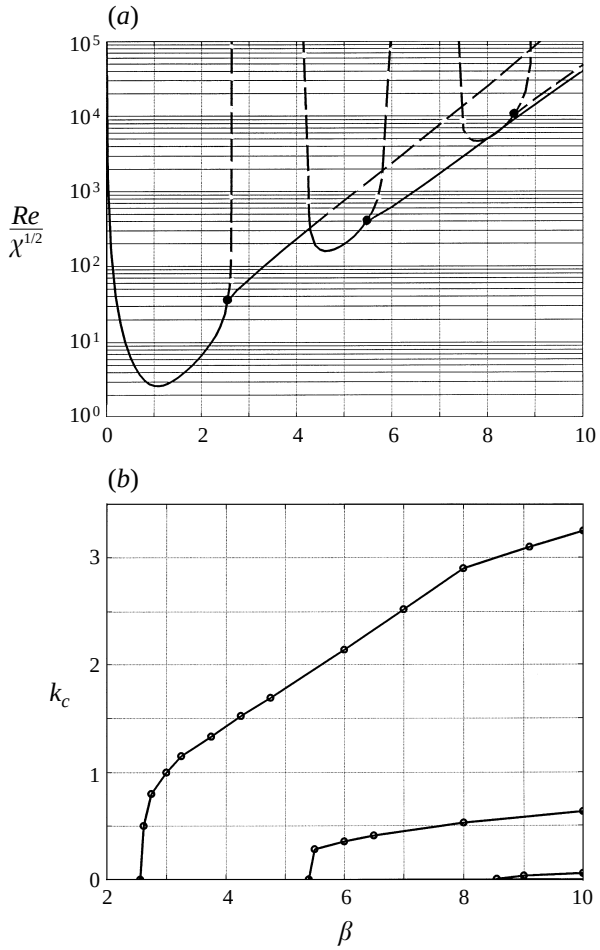

FIGURE 3. (*a*) The stability limits in the (β, Re)-plane; (*b*) the corresponding k_c for the critical finite-wavelength modes. This case has $\psi = 0.05$ and $\chi = 1.0$.

the bifurcation curve of the instability. As $k \to 0$, the stability limit tends to a value $Re_0 \approx 35.035$ which corresponds to $Re_2 = 0$, i.e. $\partial_{kk} Re = 0$ to the order considered. A branch point therefore shows where Re_2 switches sign. The branch point has a more general interpretation according to the centre-manifold description in dynamical system theory. On the neutral curve the real part of one complex Floquet exponent crosses zero. This provides a condition for a one-parameter family of neutral curves. At the branch point, the real part of a second complex Floquet exponent also crosses zero. Thus, the set of branch points is determined by two parameters. A bifurcation point that depends on two controls is of codimension two. Typically, two unstable modes whose neutral curves connect at the bifurcation point have different physical characteristics. In this case, one neutral curve has $k_c = 0$ and the other has $k_c \neq 0$ away from the branch point. The condition that $\partial_{kk} Re = 0$ at the branch point has been used to locate the branch point from the long-wavelength results. While the long-wave neutral curves do not shift with respect to ψ or χ when $Re/\chi^{1/2}$ is used as ordinate, the finite-k neutral curves, on the other hand, change with variation of these two parameters. Since the set of finite-k neutral curves emerge from the set

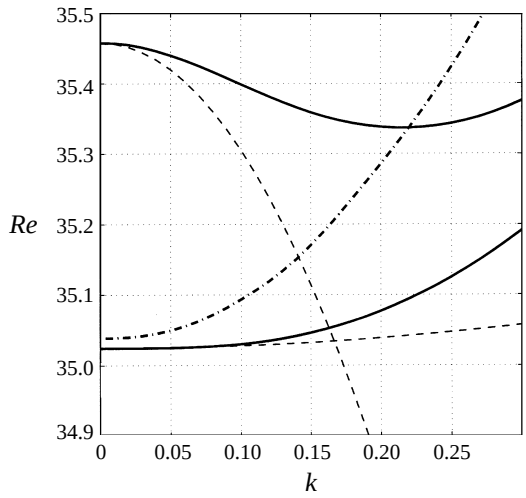

FIGURE 4. A comparison between the exact (heavy solid) and approximate (thin dashed) neutral curves. The critical curve is heavy dashed-dotted. Other parameters are $\psi = 0.05$ and $\chi = 1.0$.

of U-curves at the branch points, the behaviour of branch points with variation of ψ and χ is of interest. We now study the change of the first two branch points. In Figures 5(*a*) (first branch point) and 5(*c*) (second branch point), we show the shift in the β-position of the two branch points as both ψ and χ vary. Figures 5(*b*) and 5(*d*) basically provide the same information as 5(*a*) and 5(*c*) in terms of the values in $Re/\chi^{1/2}$. The solid, dashed and dashed-dotted lines represent the three cases $\psi = 0.5$, 0.25 and 0.025, respectively. Below (above) each curve of the branch point, Re_2 is positive (negative).

Let us first consider the behaviour of the first branch point. As shown in figures 5(*a*) and 5(*b*), the behaviour in terms of its β and $Re/\chi^{1/2}$ values is monotonic in ψ or in χ. Since χ is proportional to g, the results suggest that a larger value of gravity for a given layer thickness tends to be associated with the finite-k instability occurring at a smaller modulation amplitude. The behaviour for the variation of layer thickness at a given value of gravity is less obvious. For a small h, $\chi \to 0$ and ψ becomes large. In this situation the branch point is pushed towards the cut-off point of the U-curve and therefore corresponds to higher $Re/\chi^{1/2}$. For a large h, the effects of χ and ψ are opposite. But since χ varies as h^3 and ψ varies only as h^{-1}, the behaviour in the asymptotic case as $h \to \infty$ seems dictated by the value of χ. It seems that a thicker layer tends to make the finite-k mode more unstable in this case.

The behaviour of the second branch point is quite different from that of the first one, as shown in figures 5(*c*) and 5(*d*). Now, at a large value of χ, regardless of ψ, β appears to approach a value of 5.2 (the minimum critical point occurs at about $\beta = 4.7$) where $Re_0/\chi^{1/2}$ is about 250. But as χ tends to a smaller value before reaching zero, it is apparent that a non-monotonic behaviour can occur, depending on ψ. Such a complex variation with χ and ψ is manifested by the dashed curve at the intermediate value $\psi = 0.25$. From studying the curves, we can see that the branch point first moves down the right-hand branch of the U-curve but, short of reaching the left-hand branch, it swings back up the right-hand branch. The differences in behaviour between the first and second branch points suggest that the force balances responsible for the two bifurcation points vary.

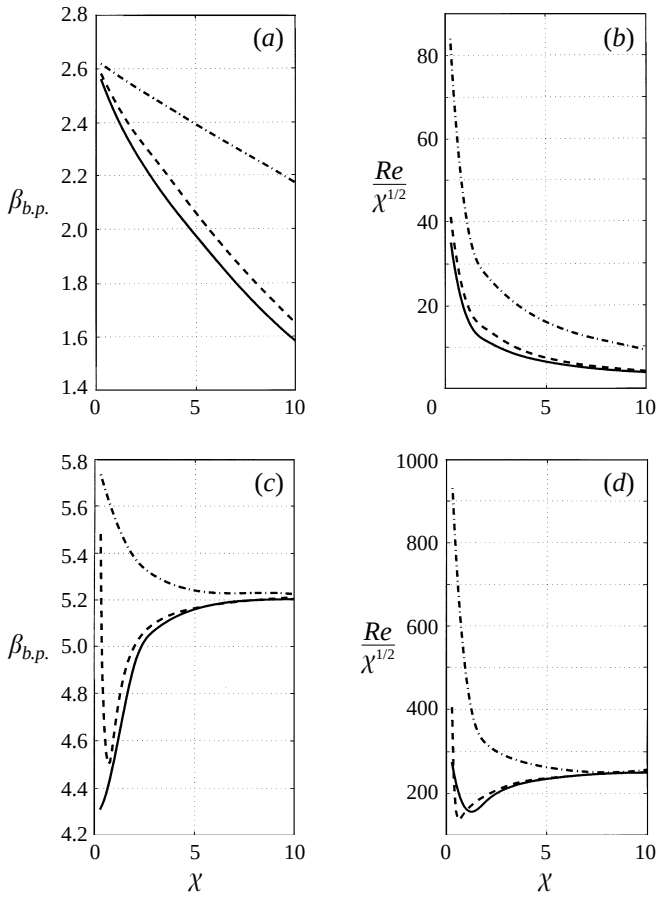

FIGURE 5. (a, c) The change of β values of the first and second branch points with χ for three ψ values: 0.025 (dashed-dotted); 0.25 (dashed) and 1.0 (solid); (a, b), and (c, d) correspond, respectively, to the first and to the second branch points of figure 2(a); figure (b) and (d) show their $Re_0/\chi^{1/2}$ values.

We now turn to the results of the second case corresponding to $\psi = 0.5$ and $\chi = 0.3$. We limit our focus to the region of the first two U-curves. Relative to the first case, we have a significantly thinner layer with weaker surface tension. In figure 6, the thin solid lines show the first two U-curves which are identical to those shown in figure 3(a) except for the vertical scale. The two solid circles represent the two branch points. The heavy solid lines are the finite-wavenumber neutral curves. The first neutral curve resembles the one in figure 3(a). The critical wavenumber associated with this curve is shown as the left-hand curve in the inserted panel in figure 6. The second heavy neutral curve is of interest here, because it emerges from the left side of the second U-curve and then turns around under it, in contrast to the situation shown in figure 3(a). By doing so it avoids going above the thin neutral curve and thereby forms a critical curve. More detailed results on this curve show that, along the curve, β first increases as it leaves the branch point, but shortly afterwards the curve encounters its first fold point and then turns left afterward. From here β starts to decrease along the curve. On the scale in figure 6, the portion of the curve near the first fold is not clearly seen (see schematic insert in figure 7 for further illustration).

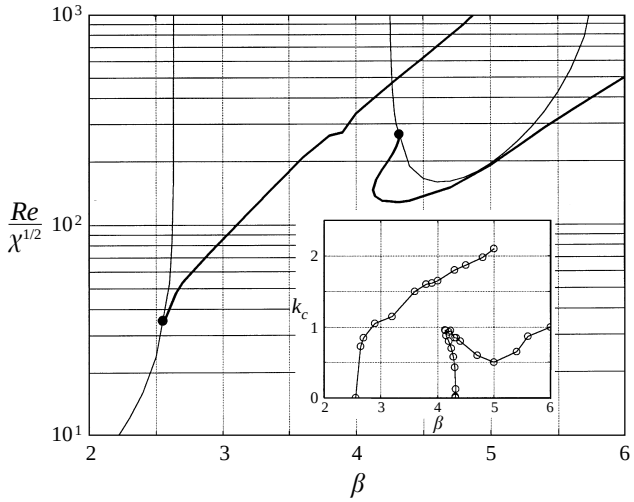

FIGURE 6. The stability limits in the (β, Re)-plane for the case $\psi = 0.5$ and $\chi = 0.3$. The solid dots again show the branch points. The thick (thin) solid lines show the finite-k (long-wave) stability limits. The inserted panel shows k_c for the finite-wavelength limits as a function of frequency.

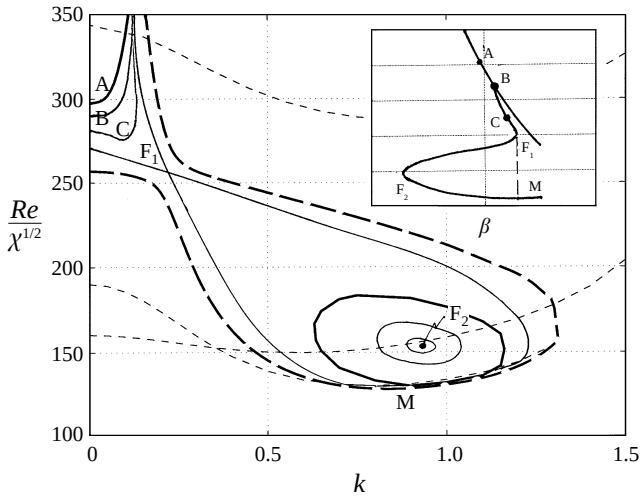

FIGURE 7. A family of neutral curves showing the pinch near the second branch point and the ring-shaped neutral curves enclosing unstable islands resulting from pinching.

As the curve continues leftward, it encounters a second fold near $\beta = 4.13$ and then turns right again. After this second turn, the curve becomes monotonic in Re as β increases. In the inserted panel, the right-hand curve shows the k_c on this second neutral curve. After increasing from zero at the second branch point, the critical wavenumber turns downward after encountering the second fold before eventually increasing again.

Further details of the shape of the neutral curves near these folds are of interest and are shown for the family of neutral curves in the (k, Re)-plane in figure 7. For clarity in interpreting these results in figure 7, we show an exaggerated version of the heavy curve in figure 5 emanating from the second branch point in the inserted panel of figure 7. Starting at the top left corner of figure 7, the outermost heavy solid curve

represents a neutral curve corresponding to point A in the inserted panel, where the line with both A and B on it is the left-hand branch of the U-curve. This neutral curve is evaluated at $\beta = 4.3$. As β increases, $(\partial_{kk} Re)_{k=0}$ decreases and eventually crosses zero right at the second branch point B. Beyond point B the U-curve is no longer the critical curve. The new critical curve is associated with a finite k_c and is shown by the curve BF_1F_2M. Between the branch point B and point F_1, it is possible for the k-family of neutral curves to have minima in Reynolds number corresponding to finite wavenumber, as shown by the thin solid line labelled C in the upper left corner region. At the first fold point, F_1, we encounter a pair of separatrices. This pair of curves is shown schematically by the thin solid lines through F_1 in figure 7. The separatrices represent the outermost curves of two k-families of neutral curves. The upper family consists of open neutral curves and the lower family consists of closed neutral curves. The minimum of the outermost curve in the upper family is at the fold F_1, which is also the maximum of the outermost curve in the lower family. The minimum of the outermost curve in the lower family is point M. As a point moves on the critical curve from point F_1 to F_2 (refer to the inserted panel), the closed neutral curves of the lower family become smaller and smaller (see schematical curves) and finally, at the second fold point F_2, the closed curve shrinks to a point. The value of β at point F_2 is about 4.13. The heavy solid closed curve shown in figure 7 is at $\beta = 4.2$. As the critical point passes point M to its right, its associated k-family neutral curve becomes open again. At $\beta = 4.32$, we show one such neutral curve in figure 7. This is the long dashed curve just outside the separatrices.

The family of pinch-shaped neutral curves and the isolated unstable islands that are associated with it is similar to a result found earlier by Pearstein (1981), in a study of the stability of a rotating doubly diffusive fluid layer (see his figure 10). In the background of figure 7, for other comparisons we also include several other neutral curves (thin-dashed). The curve with the lowest minimum is at $\beta = 4.4$. The next curve is at $\beta = 4.7$, and the uppermost curve is at $\beta = 5.4$.

Typically the set of neutral curves is obtained from a one-dimensional Newton–Raphson iteration on Re, by iterating either on k or on β. Near the folds, this iteration scheme fails to converge for obvious reasons. Then we switch to iterate on β instead, by prescribing a value for Re. But we are only interested in the minima of the family of neutral curves with respect to wavenumber, i.e. the k where $\partial_k Re = 0$. The condition $\partial_k Re = 0$ in the case of iterations on β becomes $\partial_k \beta = 0$. The latter condition is derived as follows. By differentiating $Re = Re(\beta, k)$ and keeping Re constant, we obtain

$$\frac{\partial Re}{\partial k} + \frac{\partial Re}{\partial \beta}\frac{\partial \beta}{\partial k} = 0.$$

Since $\partial_k Re$ vanishes, we expect $\partial_k \beta = 0$ unless $\partial_\beta Re = 0$.

As the number of unstable modes increases, it is important to identify the shapes of the modes. In figure 8(*a–d*), the mean field of the vertical velocity is denoted by $\overline{w}_1$ and is normalized by its maximal value. Since the flow is two-dimensional, the horizontal component of velocity can be obtained from the continuity equation. Figure 8(*a–c*) is obtained at $\psi = 0.05$ and $\chi = 1.0$ and figure 8(*d*) at $\psi = 0.5$ and $\chi = 0.3$. In figure 8(*a*), we show the $\overline{w}_1$ of the three long-wave modes at their β-minima of the three U-curves. These minima correspond to $\beta = 1.1$, 4.6 and 8.0, respectively. The first mode (see also Yih 1968) has a cantilevered shape. The second one has a single peak, whereas the last one has an asymmetric double-maxima feature. All three long-wave modes have been computed at $k = 0.01$ with the fully

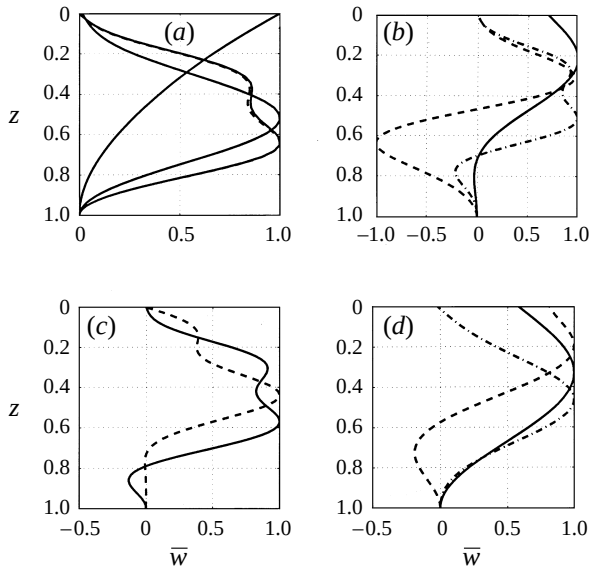

FIGURE 8. The mode shape of $\overline{w}(z)$ at neutral stability. Values of the various parameters are described in the text.

numerical method (solid). The results agree very well with the long-wave expansion (dashed): the solid and dashed curves almost overlap. The cantilever-shaped mode has maximal disturbance amplitude at the free surface. The second and third modes of disturbances, despite some minor differences, resemble a row of vortices with a very long wavelength, for which the maximal disturbance amplitude occurs near the midplane. The free surface is undisturbed by these two modes.

Figure 8(b) shows the $\overline{w}$ for the finite-wavelength modes at k_c for $\beta = 4.0$ (solid), 7.0 (dashed) and 10.0 (dashed-dotted). Although the first curve has a single maximum, the second mode has two maxima and therefore gives rise to a double row of vortices, one stacked on top of the other. The third mode in turn has two maxima and corresponds to very small k_c; in the case shown we have $k_c = 0.038$.

In figure 8(c) we show two modes corresponding to different Re (at $k = 0.03$ near their critical wavenumbers) for a large $\beta = 9.0$. One has $Re = 1.8 \times 10^4$ and the other $Re = 1.1 \times 10^5$, separated by almost an order of magnitude. The solid curve shows the finite-wavelength mode corresponding to the lower of the two Re and is similar to the one at $\beta = 10.0$ in figure 8(b). The dashed curve is on the first branch of the finite-k neutral curve.

Figure 8(d) last panel is obtained at a different set of ψ and χ. The three curves are obtained at $\beta = 2.7$ (solid), 4.0 (dashed) and 5.0 (dashed-dotted), all at the same k_c. Results in figure 8(d) shows a close resemblance to those in 8(b). In studying the mode shapes it should be emphasized that the profiles shown correspond to steady, spatially periodic flows.

6. Concluding remarks

We have identified a bifurcation point of codimension 2 on each of the U-curves corresponding to neutrally stable long waves. Each such point gives rise to an oblique critical curve associated with a finite-wavelength instability. The finite-wavelength

instability depends on surface tension effects in addition to gravity. Unlike the long-wave mode, the finite-wavelength mode occurs continuously as the imposed frequency varies and thus fills up the gaps in the unstable regions resulting from the long-wavelength analysis.

The changes among the various mean terms in the free-surface stress conditions are examined, and the dominant terms associated with Yih's long-wave mode are identified. The finite-wavelength instability is significantly more complicated as it is found that the second critical curve can exhibit folds and separatrix connection. The force balances in the two solvability conditions, as well as the mode shapes, depend very much on the imposed frequency.

I thank Professor R. E. Kelly for both support and encouragement, as well as for numerous discussions which have made this work possible and for reviewing the manuscript. Stylistic comments by the reviewers are also acknowledged. This research was supported by the NASA Microgravity Fluid Physics Program through Grant NAG3-1456.

Appendix A. On the non-existence of subharmonic solutions

Subharmonic and synchronous instabilities are both quite common among temporally modulated flows. Problems involving modulation of thermal gradient (Yih & Li, 1972) or gravitational acceleration (Clever, Schubert & Busse 1993) contain subharmonic as well as synchronous solutions. In contrast, no subharmonic solution has so far been reported in systems in which the modulation is shear-induced; see e.g. Kelly & Hu, (1994), Or & Kelly, (1995), and Schulze & Davis (1995). In this Appendix, we provide a basic argument to explain why in one case subharmonic solutions can occur but in the other case they cannot. This argument, like Floquet theory, is based solely on the basic mathematical properties of the equations and not on the detailed physics of the actual phenomena.

Through applications of numerical methods, the truncated, finite-dimensional stability problem can typically be expressed in matrix form as

$$\omega \boldsymbol{B} \frac{\mathrm{d}}{\mathrm{d}\theta} \boldsymbol{x} = \boldsymbol{A}\boldsymbol{x} + \alpha \boldsymbol{F}(\theta)\boldsymbol{x}. \tag{A 1}$$

In our present discussion, we further assume that all three matrices, $\boldsymbol{A}$, $\boldsymbol{B}$ and $\boldsymbol{F}$ are real. The phase angle $\theta = \omega t$, rather than time, is used as the independent variable here, where ω is the imposed frequency. We focus our discussion on two cases now: $\alpha = 1$, which represents systems with real coefficients, e.g. due to modulation of the basic temperature or gravity; and $\alpha = \sqrt{-1}$, which represents the system studied here as well as other shear-modulated stability problems. When the stability results are symmetric about $Re = 0$, i.e. for $Re > 0$ and $Re < 0$, these two cases are identical to the cases $\alpha = -1$ and $\alpha = -\sqrt{-1}$.

In (A 1), all matrices except $\boldsymbol{F}(\theta)$ are constant; $\boldsymbol{F}(\theta)$ is time-periodic, satisfying the following condition

$$\boldsymbol{F}(\theta \pm \pi) = -\boldsymbol{F}(\theta). \tag{A 2}$$

We emphasize that (A 2) is a more stringent condition than the 2π-periodic condition; and implies a periodicity of 2π; and that the modulating force has to vanish when

averaged over a period 2π; that is,

$$\int_0^{2\pi} \boldsymbol{F}(\theta)\, \mathrm{d}\theta = \mathbf{0}.$$

The above condition is typical and implicitly assumed in most stability problems involving modulation. Floquet theory provides the mathematical form for the solution, namely

$$\boldsymbol{x}(\theta) = \hat{\boldsymbol{x}}(\theta)\, \mathrm{e}^{\sigma\theta} \tag{A 3}$$

where σ is complex equal to $\sigma_r + \mathrm{i}\sigma_i$, σ_r is the growth rate and σ_i is a second frequency that is associated with quasi-periodic motion of the system. What makes the Floquet form useful is that $\hat{\boldsymbol{x}}(\theta)$ has the same period 2π as $\boldsymbol{F}(\theta)$. Floquet theory by itself, however, does not yield stability information, nor does it impose further restrictions on the above functional form.

A general numerical procedure does not discriminate between whether (A 1) is real or complex or whether the neutral solutions should be periodic or quasi-periodic. In the general scheme, upon substituting the Floquet form into the equation, the real and imaginary parts of the resulting complex algebraic system will provide two equations for determining the two real parameters σ_r and σ_i, if all other parameters are prescribed. Examining (A 1) suggests, however, that there are situations in which there exists a certain symmetry property in the equation which imposes further restrictions on the Floquet form of solution. A restriction is a built-in redundancy in the real and imaginary parts of the Floquet form. As a result of the redundancy, a solution can only admit certain values of σ_i. Furthermore, as the real and the imaginary parts of the equation are independent, the system essentially reduces to one real equation to determine one real unknown, σ_r.

For the case $\alpha = 1$, the symmetry in (A 1) is the invariance of the equation to complex-conjugate operation. As a result, a solution can always be expressed in real form, $\sigma_i = 0$. Based on Floquet theory, over one full period we have

$$\boldsymbol{x}(\theta + 2\pi) = K\boldsymbol{x}(\theta), \tag{A 4}$$

where K is the amplification factor. Since $\boldsymbol{x}$ is real, there are two possible values of K. These are $K = \pm \mathrm{e}^{\sigma_r 2\pi}$. The positive sign corresponds to $\sigma_i = 0$ (synchronous solutions) and the negative corresponds to $\sigma_i = 1/2$ (subharmonic solutions). There is no third possibility.

The second case, $\alpha = \sqrt{-1}$, is less straightforward. Now, assuming condition (A 2) to be satisfied, (A 1) is then invariant under the combined operation of a translation of phase by π and the conjugate operation. Thus, if $\boldsymbol{x}(\theta)$ is a solution, then $\boldsymbol{x}^*(\theta + \pi)$ is a solution. Unlike in the real case, this symmetry relation is not very useful when applied directly to the Floquet form (A 3). The reason is that the solution in this case is neither real or imaginary, but complex. In this case, we direct our argument to the expansion form for periodic solutions. Basically, we will argue that there exists an expansion for synchronous solutions, but that there is no non-trivial expansion for the subharmonic solution consistent with the imposed symmetry property. In such an expansion, a synchronous solution can be represented as

$$\boldsymbol{x}(\theta) = \mathrm{e}^{\sigma_r\theta} \sum_{n=-\infty}^{\infty} \boldsymbol{x}_n\, \mathrm{e}^{\mathrm{i}n\theta}, \tag{A 5}$$

and a subharmonic solution of order 1/2 as

$$\boldsymbol{x}(\theta) = \mathrm{e}^{\sigma_r \theta} \sum_{n=-\infty}^{\infty} \boldsymbol{x}_n \, \mathrm{e}^{\mathrm{i}(n+1/2)\theta}. \tag{A 6}$$

The two expressions are obtained from the general Floquet expansion by letting $\sigma_i = 0$ and $\sigma_i = 1/2$, respectively. We note that a trivial solution with all the Fourier coefficients equal to zero is always a solution of the governing equation. We now apply the translation-conjugacy operation in turn to each of the above expansions. After regrouping terms in the resulting series, we then do a term-by-term comparison between the two series for $\boldsymbol{x}^*(\theta + \pi)$ and $\boldsymbol{x}(\theta)$, based on the relationship $\boldsymbol{x}^*(\theta + \pi) = K\boldsymbol{x}(\theta)$, where K is an arbitrary complex constant. We then obtain a set of conditions for the expansion coefficients. For the synchronous solutions, after eliminating the redundancy in the coefficients, we obtain

$$\boldsymbol{x}(\theta) = \mathrm{e}^{\sigma_r \theta} \left\{ \boldsymbol{x}_0 + \mathrm{i}(\boldsymbol{x}_{1c} \cos\theta + \boldsymbol{x}_{1s} \sin\theta) + (\boldsymbol{x}_{2c} \cos 2\theta + \boldsymbol{x}_{2s} \sin 2\theta) + \ldots \right\}, \tag{A 7}$$

where now all coefficients are real. One can now easily check that the symmetry is satisfied. In the above, the even terms are real but the odd terms are imaginary. We now turn to the subharmonic case. Again applying the translation and conjugate operations to (A 6), redefining the index so that we can cast the series into the same form as (A 6) except for the coefficients, we obtain

$$\boldsymbol{x}^*(\theta + \pi) = \mathrm{e}^{\sigma_r(\theta+\pi)} \sum_{n=-\infty}^{\infty} \left\{ \boldsymbol{x}^*_{-(n+1)} \, \mathrm{e}^{\mathrm{i}(n+1/2)\pi} \right\} \mathrm{e}^{\mathrm{i}(n+1/2)\theta}. \tag{A 8}$$

The above arguments now lead to the following important relationship:

$$K\boldsymbol{x}_n = \boldsymbol{x}^*_{-(n+1)} \, \mathrm{e}^{\mathrm{i}(n+1/2)\pi} \, \mathrm{e}^{\sigma_r \pi}.$$

We can absorb the factor $\mathrm{e}^{\sigma_r \pi}$ into K without loss of generality. For simplicity we also keep the same notation for K. After separating the above condition into real and imaginary parts we obtain

$$K_r \boldsymbol{x}^r_n - K_i \boldsymbol{x}^i_n = (-1)^n \boldsymbol{x}^i_{-(n+1)}, \tag{A 9a}$$

$$K_r \boldsymbol{x}^i_n + K_i \boldsymbol{x}^r_n = (-1)^n \boldsymbol{x}^r_{-(n+1)}, \tag{A 9b}$$

with the superscripts r, i denoting the real and imaginary parts, respectively. The set of conditions is true for an arbitrary integer n. Now we consider two indices, $n = 0, -1$. At $n = 0$, we obtain

$$K_r \boldsymbol{x}^r_0 - K_i \boldsymbol{x}^i_0 = \boldsymbol{x}^i_{-1}, \quad K_r \boldsymbol{x}^i_0 + K_i \boldsymbol{x}^r_0 = \boldsymbol{x}^r_{-1}. \tag{A 10}$$

At $n = -1$, we obtain instead

$$K_r \boldsymbol{x}^r_{-1} - K_i \boldsymbol{x}^i_{-1} = -\boldsymbol{x}^i_0, \quad K_r \boldsymbol{x}^i_{-1} + K_i \boldsymbol{x}^r_{-1} = -\boldsymbol{x}^r_0. \tag{A 11}$$

Using (A 10) to eliminate the terms $\boldsymbol{x}^r_{-1}$ and $\boldsymbol{x}^i_{-1}$ in (A 11), we obtain

$$(K_r^2 + K_i^2 + 1)\boldsymbol{x}^r_0 = 0, \quad (K_r^2 + K_i^2 + 1)\boldsymbol{x}^i_0 = 0, \tag{A 12}$$

which implies $\boldsymbol{x}^r_0 = \boldsymbol{x}^i_0 = 0$. Similarly, we conclude that $\boldsymbol{x}^r_{-1} = \boldsymbol{x}^i_{-1} = 0$. The above results along with conditions (A 9a, b) give the trivial solution, one with all coefficients equal to zero. Thus, the subharmonic expansion can only admit the solution $\boldsymbol{x} = 0$.

Before we end the discussion, we note two important points. (i) When $\boldsymbol{A}$ or $\boldsymbol{B}$ is complex, it is certainly possible that this complex configuration with a real

modulation matrix can fall within our discussion for the case $\alpha = 1$ of real matrices. If the complex system contains a real eigenvalue, it is possible that the complex system resembles our real case of $\alpha = 1$ when transformed to the eigensubspace. Therefore it not surprising to notice that subharmonic solutions can exist, for example, in Woods & Lin's (1995) model, in which $\boldsymbol{A}$ is complex due to the presence of mean shear. One of the eigenmodes possessed by their system represents Faraday waves, which can be subharmonics. (ii) The argument depends solely on the expansion form and the symmetry condition. It does not depend on such details as whether the unmodulated eigenmode is monotonic or oscillatory.

Appendix B. A matrix iterative method

Here we provide an iterative scheme for solving (A 1). We note $\omega = 2\beta^2$ and $\alpha = \sqrt{-1}$ and replace $\boldsymbol{F}(\theta)$ by $Re(\boldsymbol{F}_c \cos\theta + \boldsymbol{F}_s \sin\theta)$. According to Floquet theory, a general response $\boldsymbol{x}(\theta)$ can be expanded in the following form,

$$\boldsymbol{x}(\theta) = \sum_{n=-\infty}^{\infty} \boldsymbol{x}_n \, \mathrm{e}^{\mathrm{i}n\theta + \sigma\theta}, \tag{B 1}$$

where the $\boldsymbol{x}_n$ are constant vector coefficients and σ is the complex Floquet exponent. Along the neutral curves σ_r, the real part of σ, vanishes. In general we can always consider the imaginary part, σ_i, in the principal range $0 \leqslant \sigma_i < 1$. Direct substitution of (B 1) in (A 1) yields the following infinite set of matrix difference equations:

$$(\boldsymbol{A} - \omega(\sigma + \mathrm{i}n)\boldsymbol{B})\boldsymbol{x}_n = -Re(\boldsymbol{F}^* \boldsymbol{x}_{n-1} + \boldsymbol{F}\boldsymbol{x}_{n+1}), \; n = -\infty, .., 0, ..\infty, \tag{B 2}$$

where

$$\boldsymbol{F} = \tfrac{1}{2}(\boldsymbol{F}_c + \mathrm{i}\boldsymbol{F}_s),$$

and $\boldsymbol{F}^*$ denotes its complex conjugate. The infinite set of difference equations is truncated. Closure is imposed by neglecting all terms outside the range of the two terms $\boldsymbol{x}_{-(N_p+1)}$ and $\boldsymbol{x}_{(N_p+1)}$ in the series. Augmenting the truncated set will still yield a large matrix eigensystem. The augmented matrices possess a block-tridiagonal property, which suggests that the set of difference equations can be treated by a direct successive elimination procedure.

At $n = N_p$, we have

$$\boldsymbol{x}_n = \boldsymbol{R}_n \boldsymbol{x}_{n-1}, \quad \boldsymbol{R}_n = -Re(\boldsymbol{A} - \omega(\sigma + \mathrm{i}n)\boldsymbol{B})^{-1}\boldsymbol{F}^*. \tag{B 3}$$

First, by proceeding with a backward substitution beginning at $n = N_p - 1$ and ending at $n = 1$, we obtain the following sequence of equations:

$$\boldsymbol{x}_n = \boldsymbol{R}_n \boldsymbol{x}_{n-1}, \quad \boldsymbol{R}_n = -Re(\boldsymbol{A} - \omega(\sigma + \mathrm{i}n)\boldsymbol{B} + Re\boldsymbol{F}\boldsymbol{R}_{n+1})^{-1}\boldsymbol{F}^*. \tag{B 4}$$

At $n = 1$ the final equation is $\boldsymbol{x}_1 = \boldsymbol{R}_1 \boldsymbol{x}_0$. Second, the forward substituion starts at $n = -N_p$, which gives

$$\boldsymbol{x}_n = \boldsymbol{R}_n \boldsymbol{x}_{n+1}, \quad \boldsymbol{R}_n = -Re(\boldsymbol{A} - \omega(\sigma + \mathrm{i}n)\boldsymbol{B})^{-1}\boldsymbol{F}. \tag{B 5}$$

The forward substitution starts at $n = -N_p + 1$ and ends at $n = -1$. It gives the sequence of equations,

$$\boldsymbol{x}_n = \boldsymbol{R}_n \boldsymbol{x}_{n+1}, \quad \boldsymbol{R}_n = -Re(\boldsymbol{A} - \omega(\sigma + \mathrm{i}n)\boldsymbol{B} + Re\boldsymbol{F}\boldsymbol{R}_{n-1})^{-1}\boldsymbol{F}. \tag{B 6}$$

The final equation is $\boldsymbol{x}_{-1} = \boldsymbol{R}_{-1} \boldsymbol{x}_0$. Both chains have length N. The $n = 0$ equation

from the original sequence is

$$(\boldsymbol{A} - \omega\sigma\boldsymbol{B})\boldsymbol{x}_0 = Re(\boldsymbol{F}^*\boldsymbol{x}_{-1} + \boldsymbol{F}\boldsymbol{x}_1).$$

After eliminating $\boldsymbol{x}_{\pm 1}$ in the $n = 0$ equation, we obtain a homogeneous equation governing $\boldsymbol{x}_0$,

$$\{\boldsymbol{A} - \omega\sigma\boldsymbol{B})\boldsymbol{x}_0 + Re(\boldsymbol{F}^*\boldsymbol{R}_{-1} + \boldsymbol{F}\boldsymbol{R}_1)\}\,\boldsymbol{x}_0 = 0, \tag{B 7}$$

which admits a non-trivial solution if the determinant vanishes. Now, we can either determine a real parameter on the neutral curves as well as the value of σ_i, or we can imposed all the parameter values and determine the growth rate as well as the modulation frequency.

In the actual numerical implementation we used, the above complex scheme has been reduced to a real scheme, by restricting to either the synchronous ($\sigma_i = 0$) or the subharmonic ($\sigma_i = 1/2$) responses. A subharmonic scheme has actually been incorporated to search for subharmonic solutions by numerical means. The result obtained so far indeed confirms the conclusion of Appendix A.

REFERENCES

Clever, R., Schubert G. & Busse, F. H. 1993 Two-dimensional oscillatory convection in a gravitationally modulated fluid layer. *J. Fluid Mech.* **253**, 663–680.

Coward, A. V. & Renardy, Y. Y. 1995 Small amplitude oscillatory forcing on two-layer plane channel flow. *Bull. Am. Phys. Soc.* **40**, 1950.

Gottlieb, D. & Orszag, S. A. 1981 *Numerical Analysis of Spectral Methods: Theory and Applications.* SIAM, Philadelphia.

Joseph, D. D. & Renardy, Y. Y. 1993 *Fundamentals of Two-Fluid Dynamics.* Springer.

Kelly, R. E., Goussis, D. A., Lin, S. P. & Hsu, F. K. 1989 The mechanism for surface wave instability in film flow down an inclined plane. *Phys. Fluids* A **1**, 819–828.

Kelly, R. E. & Hu, H. C. 1994. The effect of finite amplitude nonplanar flow oscillations upon the onset of Rayleigh-Bénard convection. *Heat Transfer 1994, Proc. 10th Intl Heat Transfer Conf.*, vol. 7, pp. 79–83.

Lin, S. P., Chen, J. N. & Woods, D. R. 1996 Suppression of instability in a liquid film flow. *Phys. Fluids* (Submitted).

Or, A. C. & Kelly, R. E. 1995*a* Finite wavelength instability of a free surface due to an oscillatory shear flow. *Bull. Am. Phys. Soc.* **40**, 1949.

Or, A. C. & Kelly, R. E. 1995*b* Onset of Marangoni convection in a layer of fluid modulated by a weak nonplanar oscillatory shear. *Intl J. Heat Mass Transfer* **38,** 2269–2279.

Pearlstein, A. J. 1981 Effect of rotation on the stability of a doubly diffusive fluid layer. *J. Fluid Mech.* **103**, 389–412.

Schulze, T. P. & Davis, S. H. 1995 Shear stabilization of morphological instability during directional solidification. *J. Cryst. Growth* **149**, 253–265.

Smith, M. K. 1990 The mechanism for the long-wave instability in thin liquid films. *J. Fluid Mech.* **217**, 469–485.

Woods, D. R. & Lin, S. P. 1995 Instability of a liquid film flow over a vibrating inclined plane. *J. Fluid Mech.* **294**, 391–407.

Yih, C. S. 1963 Stability of liquid flow down an inclined plane. *Phys. Fluids* **6**, 321–334.

Yih, C. S. 1968 Instability of unsteady flows or configurations Part 1. Instability of a horizontal liquid layer on an oscillating plane. *J. Fluid Mech.* **31**, 737–751.

Yih, C. S. & Li, C. H. 1972 Instability of unsteady flows or configurations Part 2. Convective instability, *J. Fluid Mech.* **54**, 143–152.